MoS_2/Au sensitized TiO_2 nanotube arrays with core-shell nanostructure for hydrogen production

Xiao-Rong Cheng*, [a], Yu-Hua Lu[b], Graham Dawson*, [c],

[a]Suzhou Institute of Industrial Technology,
Suzhou, Jiangsu 215104, P. R. China
[b]Jiangsu Key Laboratory of Thin Films and Department of Physics,
Soochow University, Suzhou, Jiangsu 215006,P. R. China
[c]Department of Chemistry, Xi'an Jiaotong Liverpool University, Suzhou, 215123, PR China

ABSTRACT: Herein, a TiO_2 NTAs-Au-MoS_2 core-shell photoanode was constructed with the intention to fulfill the efficient transfer of photo-generated carriers to the photoelectrode's surface. Au nanoparticles were decorated by a drop casting method and the MoS_2 layer was deposited above the Au nanoparticles using a photoreduction-annealing process. Au nanoparticles were well dispersed on the inner wall of the TiO_2 nanotubes and covered by MoS_2 layer, forming a core-shell nanostructure. The MoS_2 layer significantly improved the attachment between Au nanoparticles and TiO_2 NTAs resulting in increased PEC stability and performance. Attributed to the excitation of Au nanoparticles' LSPR effect and visible light utilization of MoS_2, the TiO_2 NTAs-Au-MoS_2 core-shell photoanode exhibits greatly enhanced photocurrent density. An increase from 67 $\mu A/cm^2$ to 234 $\mu A/cm^2$ under Xe lamp illumination and from 2.6 $\mu A/cm^2$ to 12.6 $\mu A/cm^2$ under visible light illumination (λ>420 nm) compared with the TiO_2 NTAs was observed.

KEY WORDS: nanostructures; photoelectrochemical property; hydrogen production

INTRODUCTION

In recent years, semiconductor photocatalysts have attracted great scientific interesting for their relevance to renewable energy storage and potential for providing energy without the emission of carbon dioxide [1]. Photoelectrochemical (PEC) water splitting on semiconductor photocatalysts is a prospective solution for fulfilling this purpose [2, 3]. Since Fujishima *et al.* reported n-type titanium dioxide (TiO_2) as a photocatalyst for water splitting [4], TiO_2 has been widely researched due to its remarkable stability in electrolyte, high photocatalytic ability and low cost [5]. However, the applications of TiO_2 as photocatalyst are still limited by its wide bandgap (only photo-responsive under UV illumination) and poor photo-generated carrier separation [6]. Recently, one dimensional (1D) TiO_2 nanotubes and vertically oriented TiO_2 nanotube arrays (TiO_2 NTAs) have attracted much attention for their highly ordered surface morphology and improved photocatalytic activity compared with traditional TiO_2 films and nanoparticles [7,8]. Molybdenum sulfide (MoS_2), as one kind of layered transition metal dichalcogenides, has been identified as one of the most attractive candidates for photocatalysis due to its catalytically active over a wide range of pH values, excellent morphologies, visible light response and good electronic properties [9]. To date, MoS_2 catalysts have been incorporated with other semiconductors by different methodologies such as: drop casting [10], electrodeposition [11], sulfidization of Mo or thermal decomposition [12]. Heterostructures with good photocatalytic properties have been successfully synthesized by coupling MoS_2 with energy band matched semiconductors such as CdS [13], MoO_3 [14] and SnO_2 [15]. In particular, an enhanced photocatalytic 3D hierarchical heterostructure was reported by coating a MoS_2 nanosheet layer on to TiO_2 nanobelts [16]. Tandem photoelectrodes comprising a wider bandgap semiconductor and a smaller bandgap one

connected in series, just like the TiO_2/MoS_2 heterostructures, have been shown to be efficient for improving the utilization of solar light. However, the photocurrent is usually limited due to the blocked transfer of photo-generated carriers at the interface between the semiconductors. Noble metal gold nanoparticles (Au NPs) with localized surface plasmon resonance (LSPR) effect have been proposed to enhance the efficiency of photo-generated carriers' transfer, such as reported in WS_2-Au-$CuInS_2$, ITO-Au-PZT, CdS-Au-$SrTiO_3$, and Au-$SrTiO_3$ photocatalysts recently [17-21].

These previous literature works have motivated us to combine MoS_2 with TiO_2 NTAs to improve the photocurrent under visible light and apply Au NPs to enhance the transfer of the photo-generated carriers at the TiO_2/MoS_2 interface. Therefore, we have constructed a TiO_2 NTAs-Au-MoS_2 photoelectrode by anodization, drop casting and photoreduction-annealing methods. The TiO_2 NTAs-Au-MoS_2 photoelectrode shows a core-shell nanostructure and a considerable enhancement of photocurrent. The coating of MoS_2 also forms a bound layer, which significantly improved the attachment between Au NPs and TiO_2 NTAs results in improved PEC stability and performance.

EXPERIMENTAL

Preparation of TiO_2 NTAs, TiO_2 NTAs-Au, TiO_2 NTAs-MoS_2 and TiO_2 NTAs-Au-MoS_2 photoelectrodes

TiO_2 NTAs were fabricated by anodization of titanium (Ti) sheets similar to the previously reported method [22]. Prior to anodization, Ti sheets (>99% purity, 15×15 mm^2) of 0.1 mm thickness were chemically etched in a mixed solution (HF : HNO_3 : H_2O=1 : 4 : 5 in volume ratio) for 3 min, followed by rinsing with deionized (DI) water. The etched Ti sheets were then ultrasonically cleaned in acetone, ethanol, DI water for 10 min each. Andization was performed in a two-electrode cell with a Ti sheet as anode and a graphite sheet as cathode. The electrodes were parallelly immersed in about 100 ml ethylene glycol (EG) solution containing 3 vol% H_2O and 0.3 wt% NH_4F at a distance of 6 cm. 60 V of voltage was applied between the electrodes for 2 hours by a DC power supply. After anodization the Ti sheets were cleaned with DI water and dried in air. The Ti sheets were then annealed in an oven at 450 ^{0}C for 3 hours with a heating rate of 1 ^{0}C /min under air atmosphere.

For TiO_2 NTAs-Au, the Au NPs were deposited on the Ti sheets (after anodization but without annealing process) by a drop casting method. About 50 μL of the Au NPs (Sigma-Aldrich, 99.99% purity) solution (20 mM) was dropped onto the Ti sheet and dried at 80 ^{0}C in air. After that, the Ti sheets with Au NPs were annealed in an oven at 450 ^{0}C for 3 hours under air atmosphere. After the annealing process, Au NPs were formed within the wall and on the surface of the TiO_2 NTAs; we call this TiO_2 NTAs-Au photoelectrode.

The MoS_2 layer was synthesized by a photoreduction-annealing process on the TiO_2 NTAs-Au. First, a bath solution consisting of 0.017 M aqueous solution of $(NH_4)_2[MoS_4]$ was prepared by adding 44 mg $(NH_4)_2[MoS_4]$ (Alfa Aesar, 99.95% purity) into 10 mL N,N-dimethylformamide (DMF). The as-prepared $(NH_4)_2[MoS_4]$ solution was sealed in a dark bottle and kept under Argon atmosphere until use. Before coating, the $(NH_4)_2[MoS_4]$ solution was sonicated for 10 min and the TiO_2 NTAs-Au samples were put on a conductive sample stage. Approximately 0.5 mL of $(NH_4)_2[MoS_4]$ solution was dropped onto TiO_2 NTAs-Au surface. Then, the sample was irradiated under 300 W Hg lamp illumination for 15 min. To exclude the high-energy irradiation from Hg lamp, an optical low pass filter with a cut-off of 400 nm was used. Subsequently, the sample was annealed at 400 ^{0}C in a nitrogen atmosphere (3 Pa) for 2 hours to form the TiO_2 NTAs-Au-MoS_2 core-shell photoelectrode. As control samples, the TiO_2 NTAs-MoS_2 was prepared by coating MoS_2 layer on the TiO_2 NTAs by the same photoreduction-annealing process.

Photoelectrochemical measurement

For PEC measurements, all the photoelectrode samples were cut into 1.5 ×1.5 cm^2 squares. Tinned copper wire

was connected to the Ti sheet substrate by gallium-indium eutectic (Sigma-Aldrich). The exposed backside and edges of the samples were sealed with an industrial epoxy (PKM12C-1, Pattex). The Photocurrent density-time (J-t) curves of the photoelectrodes were measured by an electrochemical workstation (CHI660D, CH Instrument) with a Xe lamp (Oriel, Newport Co.) as light source and 0.1 M Na_2SO_4 solution as electrolyte. The photo response was evaluated under chopped light irradiation with a long pass filter (cut-off wavelength: 420 nm) to simulate visible illumination. The intensity of the light source was calibrated with a spectroradiometer (Newport 1918) to simulate AM 1.5 illumination (100 mW/cm^2). During the measurement, photoelectrodes served as working electrode, platinum (Pt) wire as the counter electrode and an Ag/AgCl electrode as the reference electrode. The photocurrent was measured under zero applied bias voltage.

Sample characterization

The samples were characterized by a Rigaku D/MAX 3C X-ray diffractometer using Cu K_α radiation. Scanning electron microscope (SEM) surface and cross-section images of samples were observed by a Hitachi SU8010 Field-Emission SEM and transmission electron microscopy (TEM, FEI Tecnai G2F20) at an accelerating voltage of 200 kV. The X-ray photoelectron spectroscopy (XPS) analysis was performed at room temperature using a spectrometer hemispherical analyzer (ESCALAB 250Xi, Thermo). All XPS microprobe with binding energies were referenced to adventitious carbon at 284.6 eV. UV-vis absorption spectra was measured on an Agilent Cary 300 spectrometer.

Hydrogen evolution measurement

The hydrogen evolution by water splitting was conducted in an air-tight photo-reactor made of quartz glass. In the photo-reactor, the sample photoelectrode and the Pt counter electrode were separated in different tubular chambers, which avoid the mixing of hydrogen generated on the Pt electrode and oxygen on the photoelectrode. The measurement was conducted in a solution containing 0.1 M Na_2SO_4 under 100 mW/cm^2 Xe lamp illumination. The amount of hydrogen was determined by gas chromatography equipped with TCD (Tianmei, GC 7890T). The Faradic efficiency for the hydrogen production is calculated by dividing the determined amount of hydrogen into half the amount of electrons passed through outer circuit during the water splitting reaction.

RESULTS AND DISCUSSION

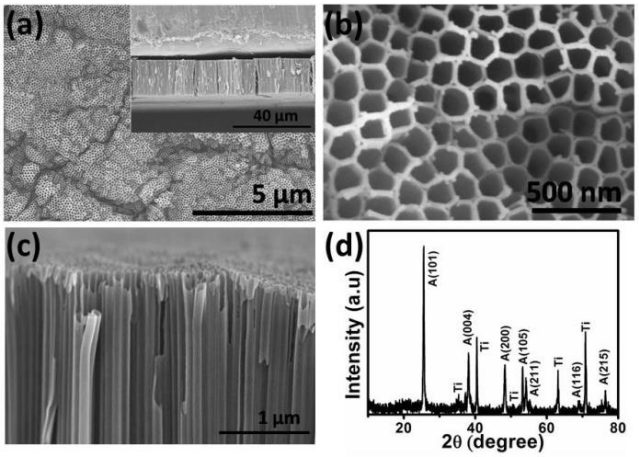

Fig. 1. Top-down (a) and (b), cross sectional (c) SEM images of TiO_2 NTAs. (d) XRD pattern of TiO_2 NTAs.

Morphological characterization and X-ray diffraction

Fig. 1(a) and (b) presents the top-down view SEM images of the TiO_2 NTAs. The TiO_2 NTAs exhibits

vertically oriented tubular array with an average diameter of about 120 nm and a wall thickness of 10 nm. The morphology features of the TiO_2 NTAs fabricated by anodization were the same as previously reported [22]. From the cross-sectional SEM image shown in the inset of Fig. 1(a), we can see the length of the open on top TiO_2 NTAs is about 20 μm. Highly ordered and aligned nanotubes with well-defined tubular structures and smooth walls can be clearly observed in Fig. 1(c). As we can see in Fig. 1(d), the TiO_2 NTAs shows obvious diffraction peaks assigned as (101), (004), (200), (105) together with some weak peaks assigned (211), (116) and (215), which are in good agreement with the standard JCPDS cards No. 21-1272 and match the characteristics of anatase phase TiO_2.

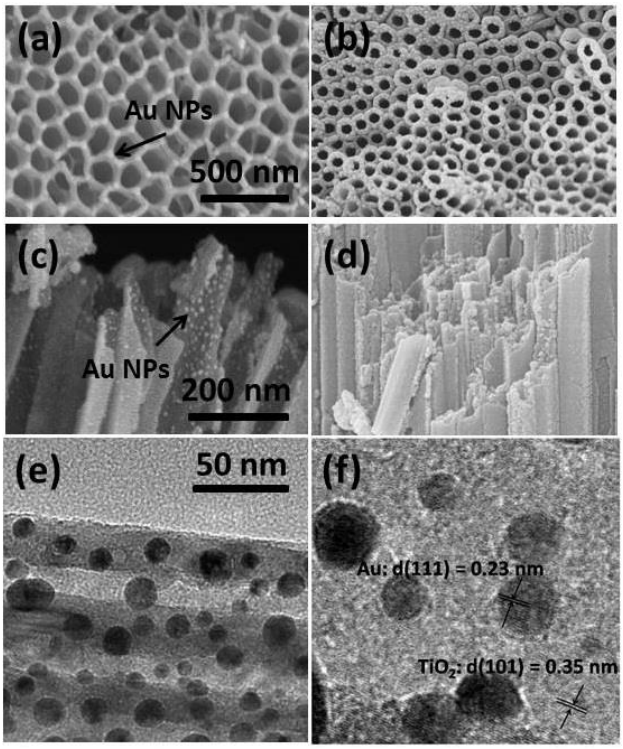

Fig. 2. Top-down and cross sectional SEM image of (a), (c) TiO_2 NTAs-Au and (b), (d) TiO_2 NTAs-Au-MoS_2. (e), (f) TEM images of TiO_2 NTAs-Au.

Fig. 2(a) and (c) show the distribution of Au NPs on the wall of TiO_2 NTAs. The fine Au NPs are highly dispersed on the inner wall of tubes which is much clearer in the TEM image of Fig. 2(e). The Au NPs can be clearly observed with good uniformity in the distribution (diameters from 10 nm to 20 nm). From the High-resolution TEM (HRTEM) image as shown in Fig. 2(f), the (111) planes of Au NPs with a lattice spacing of 0.23 nm were observed. The (101) planes of TiO_2 NTAs with a lattice spacing of 0.35 nm were also easily observed in this image. During our experiment, the deposition of Au NPs is fabricated by a drop casting and annealing process. As TiO_2 NTAs has a much larger pore size than the diameter of Au NPs, the Au NPs can move into the TiO_2 tubes. Besides, during the annealing process, the Au NPs acquired thermal energy and were able to migrate, which is governed by the surface energies at interfaces. At the final equilibrated state, the surface attains the morphology with the smallest possible surface area to volume ratio. That is why the Au NPs dispersed on the inner wall rather than aggregating on the top and blocking the tubes. As for TiO_2 NTAs-Au-MoS_2, the wall of nanotubes roughened and the mean diameter of nanotubes decreased (about 60 nm), but retained the open top. A uniform and well-attached MoS_2 layer stacked around the tube mouth as we can see in Fig. 2(b). In Fig. 2(d), a thin layer of continuous MoS_2 is formed on the inner tube wall and fully covers the tube inner surface, which reveals that the photoreduction-annealing process does not damage the ordered TiO_2 NTAs structures but forms core-shell nanostructure.

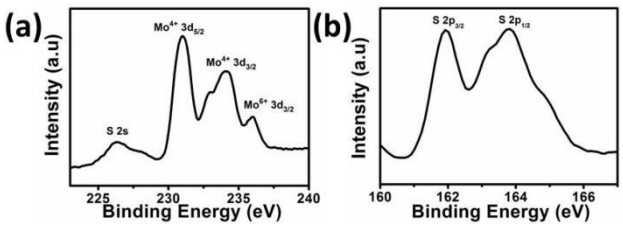

Fig. 3. XPS spectra of (a) Mo 3d and (b) S 2p of MoS_2 in TiO_2 NTAs-Au-MoS_2.

XPS analysis

The XPS analysis for MoS_2 layer in TiO_2 NTAs-Au-MoS_2 fabricated by a photoreduction-annealing process is performed and presented in Fig. 3(a) and (b), which further confirms the composition of TiO_2 NTAs-Au-MoS_2 core-shell photoanode. The XPS spectra peaks at 229.4 and 232.6 eV in Fig. 3(a) are related to Mo $3d_{5/2}$ and Mo $3d_{3/2}$ orbitals, respectively. S $2p_{3/2}$ and S $2p_{1/2}$ orbitals of divalent sulfide ions (S^{2-}) at 161.5 and 162.7 eV are also shown Fig. 3(b). This results are in good agreement with the reported values for MoS_2 [12, 23, 24]. The peak of 6^+ oxidation state of Mo can be found at 235.9 eV, which can be attributed to MoO_3 [12].

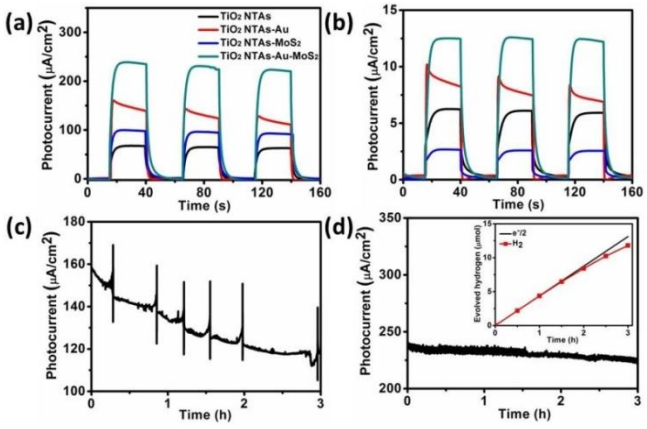

Fig. 4. J-t curves of photoelectrodes under (a) Xe lamp light (100 mW/cm^2) and (b) visible light illumination (λ>420 nm). Dependence of the photocurrent on time for (c) TiO_2 NTAs-Au and (d) TiO_2 NTAs-Au-MoS_2, inset is the hydrogen production on time measured.

PEC properties measurement and hydrogen evolution

In Fig. 4(a), we present the photocurrent density versus time (J-t) curves for the TiO_2 NTAs, TiO_2 NTAs-Au, TiO_2 NTAs-MoS_2 and TiO_2 NTAs-Au-MoS_2 photoelectrodes. The TiO_2 NTAs photoelectrode exhibits a small anodic photocurrent, 67 μA/cm^2, which is due to TiO_2 intrinsic absorption properties. As for the TiO_2 NTAs-Au, an obviously increased but gradually declining photocurrent (158 μA/cm^2 at the beginning) can be observed. The increased photocurrent is caused by the LSPR effect of Au NPs [17]. When we add a MoS_2 layer on the surface of the TiO_2 NTAs, the photocurrent increases to 98 μA/cm^2. When the Au NPs are incorporated into the interface of TiO_2 and MoS_2, an enlarged anodic photocurrent of 234 μA/cm^2 can be observed. To further understand the principle of the photocurrent increase, we measured the photocurrent of photoelectrodes using a wavelength cut-off filter of 420 nm in order to separate the contribution from the visible light where TiO_2 is not excited. Fig. 4(b) shows that the photocurrent coming from the visible light (λ>420 nm) for the TiO_2 NTAs is 2.6 μA/cm^2, which is just above the background dark current due to the weak absorption of TiO_2 NTAs in the visible region. The photocurrent increases to 9 μA/cm^2, but in a state of instability as we can see, for TiO_2 NTAs-Au. When MoS_2 layer is deposited on the TiO_2 NTAs surface, the visible light photocurrent increases to 6.2 μA/cm^2. This is

consistent with the light absorption of MoS_2, which can absorb visible light, implying in this case the photocurrent is mainly determined by MoS_2 [25]. As expected, an obvious photocurrent density enhancement is observed on the TiO_2 NTAs-Au-MoS_2 core-shell photoelectrode, reaching 12.6 μA/cm^2 under the same visible light illumination, which is nearly 5 times larger than TiO_2 NTAs. Such enhanced PEC performance originates from the following two factors: the visible light absorption of the MoS_2 layer and the presence of Au NPs at TiO_2/MoS_2 interface. Although those two factors both contribute to the enhancement of photocurrent observed, comparing Fig. 4(a) and 4(b) we believe that there are different carrier transfer mechanisms in TiO_2 NTAs-MoS_2 and TiO_2 NTAs-Au-MoS_2, which will be discussed in detail later. Fig. 4(c) shows the long time J-t curves of TiO_2 NTAs-Au. As we can see, the TiO_2 NTAs-Au exhibits unstable PEC performance, decreasing from 158 μA/cm^2 to less than 110 μA/cm^2 in 3 hours continuous PEC reaction. The main reason for this decrease of photocurrent is the loose attachment between Au NPs and TiO_2 NTAs. With the increasing PEC reaction time, the Au NPs become detached, which brings about the decrease of photocurrent density. On the other hand, a sustained photocurrent is observed for TiO_2 NTAs-Au-MoS_2 up to 3 hours of continued PEC reaction as shown in Fig. 4(d) indicating excellent stability. We believe the MoS_2 layer significantly improved the attachment between Au NPs and TiO_2 NTAs resulting in increased PEC stability. The inset figure of Fig. 4(d) shows the time course of hydrogen evolution from the TiO_2 NTAs-Au-MoS_2 core-shell photoande–Pt mesh (as cathode) electrode system. The water splitting reaction was conducted in hydrogen saturated 0.1 M Na_2SO_4 solution under 0 V *vs.* Ag/AgCl reference electrode with illumination of 100 mW/cm^2 Xe lamp. The evolution of hydrogen gas during the water splitting reaction was measured and the photocurrent during the reaction was also recorded to calculate the amount of electrons passing through the outer circuit. During the measurement, the amount of hydrogen evolved was close to half of the calculated electrons passing through the outer circuit but the Faradic efficiency slightly decreased with increasing time. In our case, the water splitting reactor is small in volume and the amount of evolved hydrogen is on the μmol scale. Such small amounts of hydrogen are quite easily dissolved in the electrolyte solution and cannot be detected by the gas chromatograph equipment. That is why the Faradic efficiency for the hydrogen production decreased to nearly 90% after 3 hours water splitting reaction.

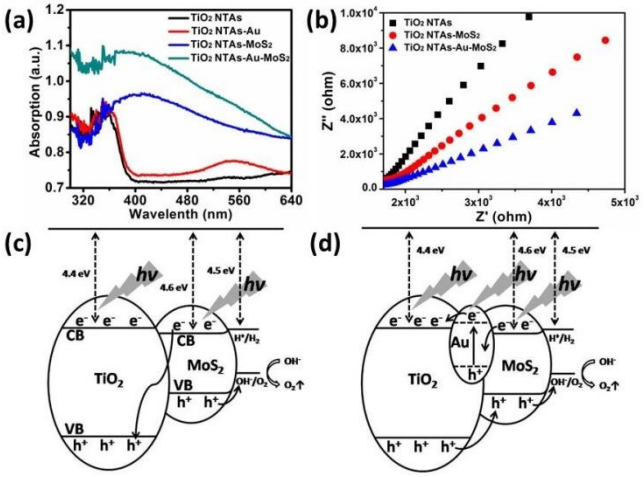

Fig. 5. (a) UV-vis absorption spectra and (b) EIS spectra of the photoelectrodes. The energy band structure of (c) TiO_2 NTAs-MoS_2 and (d) TiO_2 NTAs-Au-MoS_2.

UV-vis absorption, EIS analysis and energy band structure

To understand the observed increase of photocurrent, the UV-vis absorption spectra of different photoelectrodes were measured and compared in Fig. 5(a). The absorption spectra of TiO_2 NTAs has a clear edge around 387 nm, which corresponds to the bandgap of TiO_2 (~3.2 eV). Above the bandgap energy of TiO_2 NTAs, an

obvious enhancement of light absorption is observed with a broad peak centered around 550 nm in the absorption spectra of TiO_2 NTAs-Au. This absorption peak corresponds to the LSPR effect of Au NPs [26]. The TiO_2 NTAs-MoS_2 has obvious absorption above 360 nm, which matches the narrow bandgap of MoS_2 [25]. This implies narrow bandgap MoS_2 can improve absorption in the visible light spectrum. As for TiO_2 NTAs-Au-MoS_2, an obviously enhanced optical absorption from UV to visible light spectrum can be observed. In order to see whether the carriers' separation and transfer are enhanced at the photoelectrodes' surface simultaneously, we depict in Fig. 5(b) the corresponding electrochemical impedance spectroscopy (EIS) spectra. All the photoelectrodes show pronounced arcs at higher frequencies, whose diameters manifest the reaction rate occurring at the surface [27]. Comparing with the different photoelectrodes, the semicircle decreases with the order of TiO_2NTAs, TiO_2 NTAs-MoS_2 and TiO_2 NTAs-Au-MoS_2. As we can see, TiO_2 NTAs-Au-MoS_2 shows the smallest EIS semicircle, indicates it to be the best for carriers' separation and transfer, consistent with the observed enhanced PEC properties shown in Fig. 4(a) and (b).

On the basis of above PEC results, the schematic energy band diagrams of TiO_2 NTAs-MoS_2 and TiO_2 NTAs-Au-MoS_2 are displayed in Fig. 5(c) and (d) to illustrate the carrier migration principle. In general, TiO_2 has a wide bandgap with the conduction band (CB) and valence band (VB) edges at 4.4 and 7.6 eV below the vacuum level respectively, which can be referred to a n-type semiconductor. While MoS_2 is a narrow bandgap (~1.8 eV) n-type semiconductor with high conductivity [13, 28, 29]. The CB and VB edges of MoS_2 are located at 4.6 and 6.4 eV below the vacuum level respectively [25]. Since the CB edge of TiO_2 is situated higher than that of MoS_2, a barrier forms at TiO_2/MoS_2 interface, which impedes the photo-generated electrons moving from the CB of MoS_2 to the CB of TiO_2 as illustrated in Fig. 5(c). Upon light illumination, the photo-generated electron-hole pairs are promptly excited in both TiO_2 and MoS_2. The electrons in the CB of MoS_2 could migrate to the VB of TiO_2 and combine with the holes from TiO_2 there. This recombination of electron-hole pairs at the VB of TiO_2 acts as an electron receiver, which promotes the interfacial carriers' transfer and separation efficiency leads to the photocurrent enhancement of TiO_2 NTAs-MoS_2. Meanwhile, the electrons from the CB of TiO_2 would migrate to the bottom electrode. There is also a barrier at MoS_2/electrolyte interface. The built-in electric field induced by this barrier contributes to separation and transport of the photo-generated carriers. The holes from the VB of MoS_2 would move in the opposite direction to the electrolyte and oxidize water into oxygen, which explains the photoanodic property in TiO_2/MoS_2 composites. In this case, TiO_2 and MoS_2 are connected in series, like other tandem photoelectrode systems [30, 31], and the photocurrent is inevitably limited by the lower performing component, which in our case is MoS_2. Therefore, a relatively small photocurrent is observed as illustrated above. When TiO_2 and MoS_2 are interfaced by the Au NPs, a barrier at TiO_2/MoS_2 interface and two ohmic tunneling contacts at MoS_2/Au and TiO_2/Au interfaces are established. In this case, the photo-generated electrons from the CB of MoS_2 will migrate to Au NPs and be pumped to the CB of TiO_2 by LSPR effect. The photo-generated electrons from both MoS_2 and TiO_2 will subsequently move to the bottom electrode together as depicted in Fig. 5(d). Since the heterojunction at the TiO_2/MoS_2 interface provide a favorable energy level alignment for photo-generated holes from the VB of both TiO_2 and MoS_2, they move to the electrolyte together. In this case, the photocurrent is not be limited by MoS_2 which leads to the obviously enhanced photocurrent.

CONCLUSION

In summary, a TiO_2 NTAs-Au-MoS_2 core-shell photoanode was constructed by simple drop casting and photoreduction-annealing methods. Au NPs can restrain the combination of photo-generated electron-hole pairs and provide a stronger electron-extraction to drive the photo-generated carriers out of the photoelectrode. With the addition of the MoS_2 layer, the Au NPs are firmly attached to the TiO_2 NTAs, causing a synergistic increase in PEC performance and stability. A photocurrent density of 234 $\mu A/cm^2$ was obtained under zero bias *vs.* Ag/AgCl and

100 mW/cm^2 Xe-lamp illumination in Na_2SO_4 electrolyte, where 12.6 μA/cm^2 is from visible light illumination (λ>420 nm), which is nearly 5 times larger than that of TiO_2 NTAs. Through comparing with the PEC properties of different photoelectrodes and energy band analysis, a physical mechanism was proposed to explain the synergistic effect of MoS_2 and Au NPs.

Acknowledgements

This work was supported by Suzhou Institute of Industrial Technology research fund (Grant No. SGYKJ201705), Xi'an Jiaotong Liverpool University research development fund and National Natural Science Foundation of China (Grant No. 21650110446).

REFERENCES

1. Lewis NS and Nocera DG. *Proc. Natl. Acad. Sci. U.S.A.* 2006; **103**: 15729-15735.
2. Walter MG, Warren EL, McKone JR, Boettcher SW, Mi QX, Santori EA and Lewis NS. *Chem. Rev.* 2010; **110**: 6446-6473.
3. Cheng XR, Chen DL, Dong W, Zheng FG, Fang L and Shen MR. *Chem. Commun.* 2014; **50**: 6346-6348.
4. Fujishima A and Honda K. *Nature* 1972; **238**: 37-38.
5. Kasuga T, Hiramatsu M, Hoson A, Sekino T and Niihara K. *Adv. Mater.* 1999; **11**: 1307-1311.
6. Sun WT, Yu Y, Pan HY, Gao XF, Chen Q and Peng LM. *J. Am. Chem. Soc.* 2008; **130**: 1124-1125.
7. He H, Xiao P, zhang YH, Jia YC, Yang YN and Qiao ZY. *J. Alloys Compd.* 2012; **522**: 63-68.
8. Ye MD, Xin XK, Lin CJ and Lin ZQ. *Nano Lett.* 2011; **11**: 3214-3220.
9. Zhang LM, Liu C, Wong AB, Resasco J and Yang PD. *Nano Res.* 2015; **8**: 281−287.
10. Ding Q, Meng F, English CR, Caban-Acevedo M, Shearer MJ, Liang D, Daniel AS, Hamers RJ and Jin S. *J. Am. Chem. Soc.* 2014; **136**: 8504−8507.
11. Seger B, Laursen AB, Vesborg PCK, Pedersen T, Hansen O, Dahl S and Chorkendorff I. *Angew. Chem. Int. Ed.* 2012; **51**: 9128−9131.
12. Qi F, Li PJ, Chen YF, Zheng BJ, Liu XZ, Lan FF, Lai ZP, Xu YK, Liu JB, Zhou JH, He JR and Zhang WL. *Vacuum* 2015; **119**: 204-208.
13. Liu Y, Yu YX and Zhang WD. *J. Phys. Chem. C* 2013; **117**: 12949-12957.
14. Chen ZB, Cummins D, Reinecke BN, Clark E, Sunkara MK and Jaramillo TF. *Nano Lett.* 2011; **11**: 4168-4175.
15. Li JZ, Yu K, Tan YH, Fu H, Zhang QF, Cong WT, Song CQ, Yin HH and Zhu ZQ. *Dalton Trans.* 2014; **43**: 13136-13144.
16. Zhou WJ, Yin ZY, Du YP, Huang X, Zeng ZY, Fan ZX, Liu H, Wang JY and Zhang H. *Small* 2013; **9**: 140-147.
17. Linic S, Christopher P and Ingram DB. *Nat. Mater.* 2011; **10**: 911-921.
18. Yu SJ, Kim YH, Lee SY, Song HD and Yi J. *Angew. Chem. Int. Ed.* 2014; **53**: 11203-11207.
19. Zhong YQ, Ueno K, Mori Y, Shi X, Oshikiri T, Murakoshi K, Inoue H and Misawa H. *Angew. Chem. Int. Ed.* 2014; **53**: 10350-10354.
20. Cheng ZZ, Wang ZX, Shifa TA, Wang FM, Zhan XY, Xu K, Liu QL and He J. *Appl. Phys. Lett.* 2015; **107**: 223902.
21. Wang ZJ, Cao DW, Wen LY, Xu R, Obergfell M, Mi Y, Zhan ZB, Nasori N, Demsar J and Le Y. *Nat. Commun.* 2015; **7**: 1.
22. Kim HI, Monllor-Satoca D, Kim WY and Chio WY. *Energy Environ. Sci.* 2015; **8**: 247-257.
23. Wang L, Jie JS, Shao ZB, Zhang Q, Zhang XH, Wang YM, Sun Z and Lee ST. *Adv. Funct. Mater.* 2015; **25**:

2910-2919.

24. Gao L, Cui YC, Wang J, Cavalli A, Standing A, Vu Thuy TT, Verheijen MA, Haverkort Jos EM, Bakers Erik PAM and Notten Peter HL. *Nano Lett.* 2014; **14**: 3715-3719.
25. Kudo A and Miseki Y. *Chem. Soc. Rev.* 2009; **38**: 253-278.
26. Li JT, Cushing SK, Zheng P, Senty T, Meng FK, Bristow AD, Manivannan A and Wu NQ. *J. Am. Chem. Soc.* 2014; **136**: 8438-8449.
27. Morales-Guio CG, Liardet L, Mayer MT, David Tilley S, Grätzel M and Hu X. *Angew. Chem. Int. Ed.* 2015; **54**: 664-667.
28. Roy P, Berger S and Schmuki P. *Angew. Chem. Int. Ed.* 2011; **50**: 2904-2939.
29. Scalise E, Houssa M, Pourtois G, Afanas'ev VV and Stesmans A. *Physica E* 2014; **56**: 416-421.
30. Cheng XR, Dong W, Zheng FG, Fang L and Shen MR. *Appl. Phys. Lett.* 2015; **106**: 243901.
31. Cheng XR, Shen HY, Dong W, Zheng FG, Fang L, Su XD and Shen MR. *Adv. Mater. Interfaces* 2016; **3**: 1600485.